Chalcogenide Letters

Tech Science Press

http://doi.org/10.32604/cl.2026.083268

ARTICLE

Mixed Salt-Assisted Growth of Large-Size Ultrathin SnS_2 Nanosheets and Their Anisotropy Study

Yulong Lian[1], Ruiqiang Wang[1], Ziyan Ding[1] and Jinyang Liu[1,2,3,*]

[1]College of Physics and Energy, Fujian Normal University, Fuzhou, China
[2]Fujian Provincial Key Laboratory of Quantum Manipulation and New Energy Materials, Fuzhou, China
[3]Fujian Provincial Engineering Technology Research Center of Solar Energy Conversion and Energy Storage, Fuzhou, China
*Corresponding Author: Jinyang Liu. Email: jyliu@fjnu.edu.cn

Received: 31 March 2026; Accepted: 08 May 2026; Published: 02 June 2026

ABSTRACT: The morphological regularity, thickness uniformity, and size controllability of two-dimensional materials play a crucial role in regulating their physicochemical properties. However, achieving a synergistic balance among these three factors remains a key challenge in the field. In this study, through a systematic investigation of 36 salt-assisted growth systems, we discovered that CsCl promotes the lateral growth of SnS_2, while KI optimizes the crystal morphology. Using a CsCl/KI mixed salt system, we successfully grew triangular, ultrathin, large-area SnS_2 nanosheets with a size exceeding 200 μm and a thickness of only 1.8 nm. Angle-resolved polarized Raman spectroscopy (ARPRS) revealed that SnS_2 nanosheets transferred onto SiO_2 substrates exhibit intrinsic in-plane isotropy. In contrast, SnS_2 nanosheets grown directly on mica substrates display a 90° periodic variation in Raman peak intensity with polarization angle, indicating significant in-plane anisotropy. This anisotropy arises from interfacial stress induced by lattice mismatch between the mica substrate and SnS_2, which breaks the intrinsic symmetry of the material. In addition, the transition of SnS_2 nanosheets from in-plane optical isotropy to anisotropy were confirmed by the polarized optical microscopy characterization. These results demonstrate that the mixed salt-assisted growth strategy provides a new approach for synergistically controlling the size, shape and thickness of two-dimensional materials and offers a novel method for inducing anisotropic property in intrinsically isotropic two-dimensional materials through lattice mismatch.

KEYWORDS: Mixed salt; SnS_2 nanosheets; angle-resolved polarized Raman spectroscopy; anisotropy

1 Introduction

In recent years, two-dimensional (2D) materials with layered structures have attracted widespread attention in flexible devices, valleytronics, and optoelectronics due to their unique physicochemical properties [1,2]. The family of 2D materials is exceptionally diverse, spanning a continuous spectrum of electronic band structures. This includes zero-bandgap semimetals (e.g., graphene), narrow-bandgap semiconductors (e.g., transition metal dichalcogenides such as MoS_2 and WS_2), moderate-bandgap semiconductors (e.g., black phosphorus), and wide-bandgap insulators (e.g., hexagonal boron nitride, h-BN) [3,4]. Tin disulfide (SnS_2), an important member of the IV-VI_A group, features stacked planar triple layers with strong in-plane covalent bonding and weak out-of-plane van der Waals (vdW) interactions, making it a research hotspot [5,6]. SnS_2 is an indirect bandgap semiconductor (2.08–2.44 eV) with a light absorption efficiency exceeding 10^4 cm^{-1}, offering broad prospects in optoelectronics, gas sensing, and

photocatalysis [7,8]. Its low cost, earth abundance, non-toxicity, and environmental friendliness also align well with industrial demands for next-generation electronics and optoelectronics [9]. Thus, achieving controllable growth of 2D SnS_2 nanosheets is a primary task for advancing their applications. Currently, SnS_2 nanosheets are mainly obtained via solution-phase synthesis or mechanical exfoliation [10–12]. However, these methods typically yield small lateral sizes (several micrometers) and suffer from poor morphological uniformity, severe agglomeration, low crystallinity, or low yield, severely restricting further applications [13,14].

Chemical vapor deposition (CVD) offers precise control over morphology, defects, and structure, making it attractive for growing large-size 2D materials [15–17]. For instance, Zhou et al. [18] provided an improved CVD route to synthesize SnS_2 nanosheets with edge lengths up to 150 μm. Phototransistors based on these nanosheets showed high sensitivity (261 A/W) and fast response (20 ms rise time), but the thickness remained above 10 nm, limiting device performance. Ye et al. [19] reported the CVD growth of atomic-layer SnS_2 with a large crystal size and uniformity, and external quantum efficiency of the resultant SnS_2 crystals is as high as 150%. In addition, assisted CVD for the growth of 2D SnS_2 nanomaterials has received extensive attention recently. Wang et al. [20] synthesized in-plane SnS_2 nanosheets with sizes up to 280 μm on SiO_2/Si substrates via Te-assisted CVD, however, the shape is not regular enough, and the thickness is relatively large. Liu et al. [21] synthesized monolayer SnS_2 crystal on SiO_2/Si substrates via NaCl-assisted CVD and the edge can be as long as 80 μm, however, the shape is irregular. Shao et al. [22] introduced potassium halide into CVD and grew large-size SnS_2 nanosheets with diverse morphologies, finding that more regular morphologies tend to have greater thickness. Fu et al. [23] reported a KI-assisted confined-space CVD method to synthesize multilayer MoS_2/SnS_2 vertical heterostructure nanosheets composed of monolayer MoS_2 and multilayer SnS_2, but the thickness of SnS_2 is relatively large. During CVD growth, large-size monolayer SnS_2 growth is constrained by the high melting point of precursors and low SnS_2 adhesion on substrates [24,25]. Consequently, achieving a synergistic balance among morphological regularity, thickness uniformity, and size controllability for large-size SnS_2 growth remains a significant challenge.

In this study, a mixed salt-assisted growth strategy was employed to successfully synthesize ultrathin, large-size SnS_2 nanosheets. ARPRS and polarized optical microscopy revealed that lattice mismatch between SnS_2 and the mica substrate generates interfacial stress, breaking the intrinsic symmetry and inducing significant anisotropy. These results demonstrate that the mixed salt-assisted strategy provides a new approach for the controllable growth of 2D materials and offers a novel method for inducing anisotropy in intrinsically isotropic 2D materials via lattice mismatch.

2 Materials and Methods

2.1 Synthesis Process

A mixed salt-assisted ambient-pressure rapid chemical vapor deposition (CVD) approach was developed for synthesis of large-size, ultrathin SnS_2 nanosheets based on rapid CVD methods developed in our reports [26,27]. The typical experimental procedure to grow SnS_2 nanostructures with single salt is as follows: 0.020 g SnO_2 (Shanghai Aladdin Biochemical Technology Co., Ltd.) powder was uniformly mixed with 0.002 g KI (Shanghai Macklin Biochemical Technology Co., Ltd., 99.9% purity) to serve as the tin source. A freshly cleaved mica sheet (approximately 1 × 2 cm^2) was placed above the tin source. Sulfur powder (Shanghai Aladdin Biochemical Technology Co., Ltd.) was placed in a separate quartz boat upstream of the tin source at a certain distance. The quartz tube was evacuated and purged with argon to remove air, then backfilled to atmospheric pressure. A constant argon flow of 50 sccm was maintained, and the outlet was sealed with a water seal. When the furnace reached 540°C, the quartz tube was rapidly moved to position

the tin source at the heating center and bring the sulfur powder near the heating zone. After the reaction for 10 min, the furnace was turned off and allowed to cool to room temperature before the sample was removed. The growth process of SnS_2 nanostructures using different salts remains the same, with a constant mass ratio of SnO_2 to salt fixed at 10:1. All salts are of analytical grade and used as received without further purification (purchased from Shanghai Macklin Biochemical Technology Co., Ltd. or Shanghai Aladdin Biochemical Technology Co., Ltd.). The procedure for growing SnS_2 nanosheets with mixed salts follows the same protocol, except that a mixed salt (KI and CsCl) is used instead of a single salt. The mass ratio of SnO_2 to the mixed salt is kept constant at 10:1, while the ratio of KI to CsCl can be adjusted according to the experimental design.

2.2 Transfer Method

SnS_2 nanosheets were transferred from mica to 300 nm SiO_2/Si substrates or Cu grids by a water-assisted ultrasonic transfer as described in our previous reported [27]. The as-grown SnS_2 nanosheets were transferred onto mica to characterize polarized optical image using a mechanical transfer method. Briefly, the mica sheet carrying the as-grown SnS_2 nanosheets was brought into face-to-face contact with a freshly cleaved mica. The two substrates were gently pressed together and then slowly separated. Consequently, some SnS_2 nanosheets were transferred onto the target substrate.

2.3 Characterization

The morphology and spatial distribution of SnS_2 nanosheets were examined by reflection-mode optical microscopy (Olympus BX51M) and atomic force microscopy (AFM, Bruker Dimension Icon). Crystal structure, lattice resolution, and compositional uniformity were assessed by X-ray diffraction (XRD, Rigaku Ultima IV, Cu Kα, λ = 0.15418 nm), transmission electron microscopy (TEM, JEOL JEM-F200, 200 kV) and X-ray photoelectron spectroscopy (XPS, Thermo Fisher Scientific ESCALAB Xi, Al Kα, hν = 1486.6 eV). The polarized optical imaging was characterized using an OM equipmented with crossed polarizer and analyzer plates. Raman spectra were acquired at room temperature with a HORIBA Jobin-Yvon Evolution spectrometer using a 532 nm excitation laser kept below 5 mW to avoid sample heating.

3 Results and Discussion

3.1 Synthesis Strategy

An ambient-pressure rapid CVD method combined with a salt-assisted growth strategy was used to investigate the effects of various salt additives on the size, morphology, and thickness of SnS_2 nanosheets. Fig. 1a shows the schematic of the mixed salt-assisted rapid CVD process [26,27]. It offers several advantages, including rapid heating-up, negligible precursor loss during the heating process, and precise control over growth temperature and duration. In the absence of salt additives, only a few small and thick SnS_2 crystal are observed by optical microscopy (OM) as shown in Fig. 1b. In recent years, salts, particularly alkali metal halide salts, have been widely employed as promoters in the CVD growth of 2D materials [28,29]. While certain salts, such as NaCl and KI, have also been utilized in the CVD synthesis of SnS_2, however, the existing studies on salt-assisted SnS_2 growth remain sporadic and lack a systematic investigation. In this work, we comprehensively investigate the influence of 36 distinct salts, including alkali metal halide salts and other common salt types, on the growth of SnS_2 nanosheets (Fig. 1c). Based on careful screening and comparative analysis of these salts, an efficient mixed salt system was successfully identified and established. This optimized system enables the controllable growth of ultrathin, large-area SnS_2 nanosheets with excellent crystalline quality, providing a reliable approach for the synthesis of high-quality 2D materials.

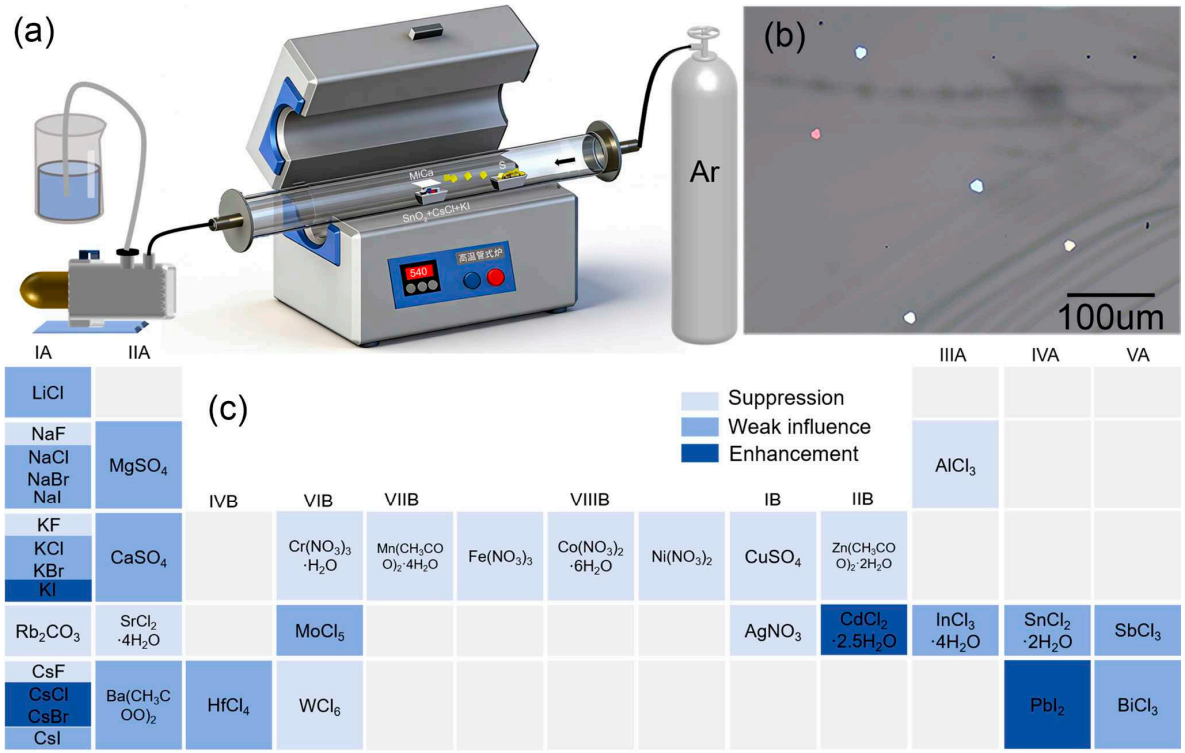

Figure 1: Schematic diagram of experiment setup and the salts used. (**a**) Schematic illustration of the mixed salt-assisted chemical vapor deposition (CVD) process, (**b**) OM images of SnS_2 nanosheets grown without salt, (**c**) Periodic table highlighting the metal salts employed in this work. Color code: light blue indicates suppressed growth; blue indicates weak influence; dark blue indicates enhanced growth.

When 12 salts such as $AlCl_3$, $Cr(NO_3)_3{\cdot}H_2O$, $Mn(CH_3COO)_2{\cdot}4H_2O$, $Fe(NO_3)_3$, $Co(NO_3)_2{\cdot}6H_2O$, $Ni(NO_3)_2$, $CuSO_4$, $Zn(CH_3COO)_2{\cdot}2H_2O$, Rb_2CO_3, $SrCl_2{\cdot}4H_2O$, WCl_6 and $AgNO_3$ were introduced into the growth system, the nucleation and subsequent growth of SnS_2 were significantly suppressed. As shown in Fig. 2, no observable SnS_2 crystal were detected on the sample surface under these conditions, indicating a complete inhibition of crystal formation. This inhibitory effect may be attributed to the strong interaction between the metal cations (such as Al^{3+}, Fe^{3+}, Rb^{+} and Ag^{+}) or their corresponding anions with the precursors or the growth substrate, which likely hinders the initial nucleation process. These results demonstrate that certain salt additives can act as growth inhibitors rather than promoters, highlighting the dual role of salts in the CVD growth of 2D materials.

The addition of 12 different salts, including LiCl, $MgSO_4$, $CaSO_4$, $MoCl_5$, $Ba(CH_3COO)_2$, $SbCl_3$, $BiCl_3$, $InCl_3{\cdot}4H_2O$, $SnCl_2{\cdot}2H_2O$, $HfCl_4$, $CdCl_2{\cdot}2.5H_2O$, and PbI_2, led to distinct morphological outcomes, as shown in Fig. 3. When salts such as LiCl, $MgSO_4$, $CaSO_4$, $MoCl_5$, $Ba(CH_3COO)_2$, $SbCl_3$, $BiCl_3$ and $InCl_3{\cdot}4H_2O$ were introduced into the precursor, only a few small SnS_2 crystals with varying brightness were observed in the OM images (Fig. 3a–h). In contrast, the addition of $SnCl_2{\cdot}2H_2O$ and $HfCl_4$ produced significantly larger SnS_2 crystals (Fig. 3i,j), suggesting that these salts may promote precursor conversion or facilitate crystal growth under identical conditions. Furthermore, the addition of $CdCl_2{\cdot}2.5H_2O$ led to the formation of multilayer SnS_2 nanosheets (Fig. 3k), indicating that $CdCl_2{\cdot}2.5H_2O$ plays a regulatory role in modulating interlayer van der Waals interactions. These weak interactions govern the vertical assembly of 2D layers, and $CdCl_2{\cdot}2.5H_2O$ appears to enable controlled layer-by-layer stacking, offering a promising route for multilayer SnS_2 synthesis. Notably, the introduction of PbI_2 induced the formation of one-dimensional (1D)

nanowires (Fig. 3l). Further analysis overturns the conventional view of PbI_2 as merely an auxiliary agent. As demonstrated by the structural and compositional analysis in Fig. S1, PbI_2 instead acts as a critical reactant, deeply participating in the lattice formation process. Consequently, the synthesized product is identified as the ternary lead-tin-sulfur compound $PbSnS_3$, not the binary tin disulfide SnS_2. These contrasting observations highlight the specificity of salt-assisted growth and underscore the importance of carefully selecting salt additives to achieve desired structural outcomes.

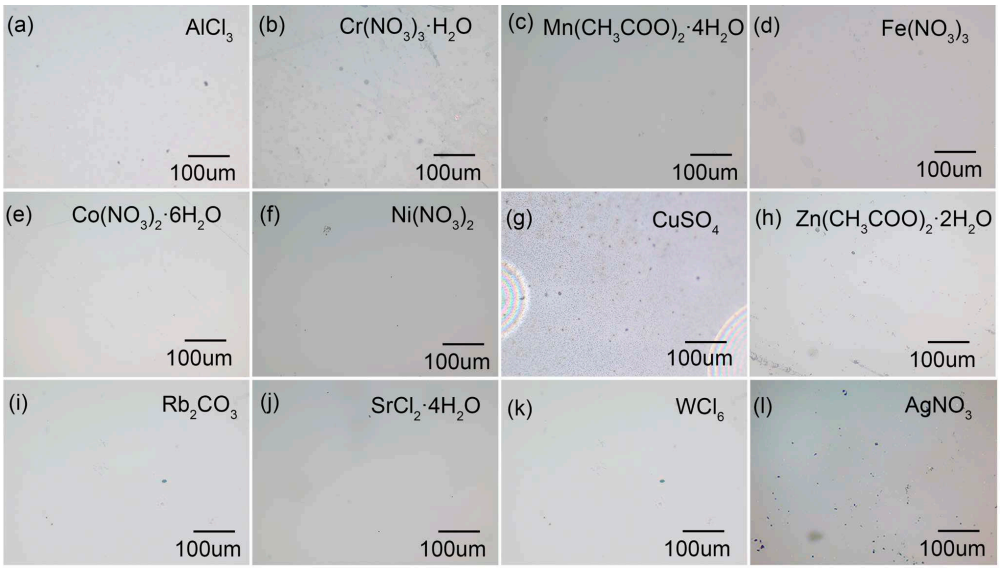

Figure 2: OM images of SnS_2 growth by salt-assisted CVD. Salts with suppression: (**a**) $AlCl_3$, (**b**) $Cr(NO_3)_3{\cdot}H_2O$, (**c**) $Mn(CH_3COO)_2{\cdot}4H_2O$, (**d**) $Fe(NO_3)_3$, (**e**) $Co(NO_3)_2{\cdot}6H_2O$, (**f**) $Ni(NO_3)_2$, (**g**) $CuSO_4$, (**h**) $Zn(CH_3COO)_2{\cdot}2H_2O$, (**i**) Rb_2CO_3, (**j**) $SrCl_2{\cdot}4H_2O$, (**k**) WCl_6 and (**l**) $AgNO_3$.

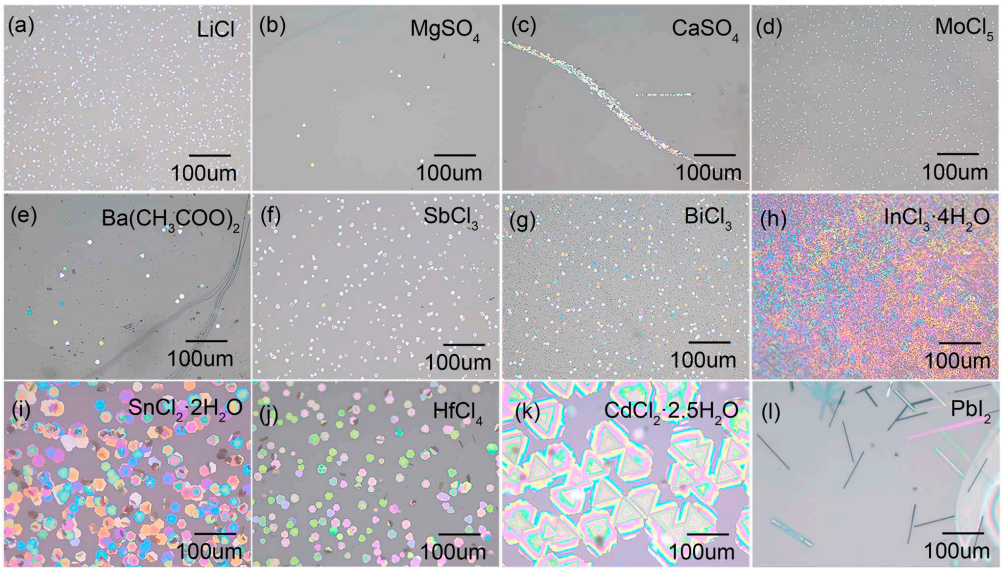

Figure 3: OM images of SnS_2 growth by salt-assisted CVD. Salts with influence: (**a**) LiCl, (**b**) $MgSO_4$, (**c**) $CaSO_4$, (**d**) $MoCl_5$, (**e**) $Ba(CH_3COO)_2$, (**f**) $SbCl_3$, (**g**) $BiCl_3$, (**h**) $InCl_3{\cdot}4H_2O$, (**i**) $SnCl_2{\cdot}2H_2O$, (**j**) $HfCl_4$, (**k**) $CdCl_2{\cdot}2.5H_2O$, and (**l**) PbI_2, respectively.

The alkali metal halide salts constitute a distinct category of additives. Within this group (NaF, NaCl, NaBr, NaI, KF, KCl, KBr, KI, CsF, CsCl, CsBr, and CsI), only CsCl, CsBr, and KI demonstrated significant regulatory capabilities in the SnS_2 growth process (Fig. 4). Specifically, both cesium salts effectively promoted lateral expansion while simultaneously suppressing vertical growth, leading to larger but thinner crystals. CsCl was more potent in this regard than CsBr; however, both yielded products with irregular morphologies. By contrast, KI primarily enhanced the crystalline quality and shape regularity of the nanosheets, although the products remained relatively thick with notable thickness variation. The remaining alkali halides showed little to no effect, with NaF, KF, CsF acting as a strong inhibitor of normal crystal development.

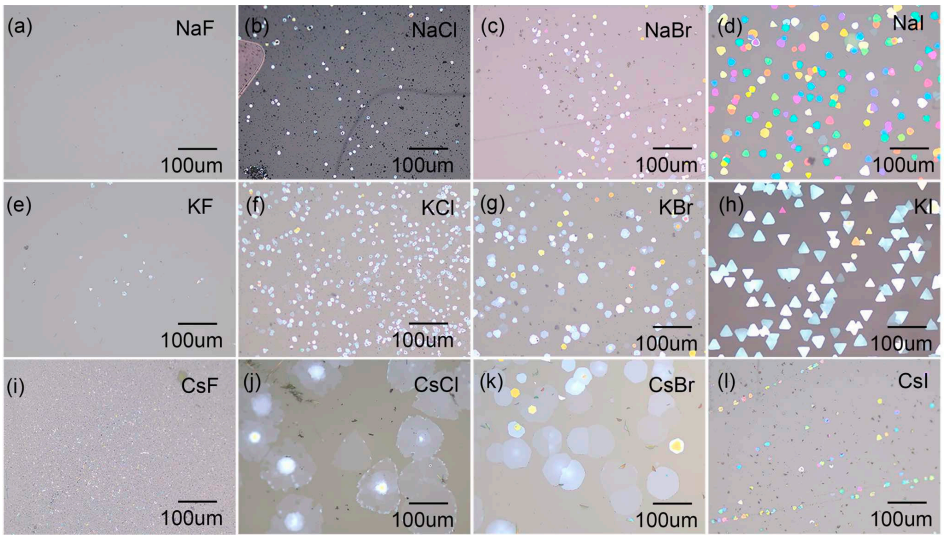

Figure 4: OM images of SnS_2 growth by salt-assisted CVD. alkali metal halide salts: (**a**) NaF, (**b**) NaCl, (**c**) NaBr, (**d**) NaI, (**e**) KF, (**f**) KCl, (**g**) KBr, (**h**) KI, (**i**) CsF, (**j**) CsCl, (**k**) CsBr and (**l**) CsI.

To better understand the effects of salts on the growth of SnS_2 nanostructures, a periodic table of the metal salts with different color scheme were draw as shown in Fig. 1c. These salts can be divided into three categories: 15 salts marked in light blue (such as $AlCl_3$, $AgNO_3$, NaF, et al.) represent suppressed growth, 16 salts marked in blue (such as LiCl, $CaSO_4$, $BiCl_3$, NaCl, et al.) represent no significant effect on growth, and 5 salts marked in dark blue ($CdCl_2{\cdot}2.5H_2O$, PbI_2, KI, CsCl and CsBr) represent enhanced growth. Most of salts had a weak influence or even suppression on growth, and only a few salts enhanced growth. Among them, CsCl significantly enhance lateral size and reduce thickness of SnS_2, while KI optimizes its crystallinity and morphology. This classification strategy enables intuitive screening of auxiliary growth agents with potential application value, providing new insights for the controllable preparation of 2D materials.

To elucidate the synergistic mechanism of CsCl and KI and the effects of their mixing ratio on the growth morphology, size, thickness, and crystalline quality of SnS_2, a series of comparative experiments was designed based on single salt-assisted growth shown above. The CsCl/KI ratio was systematically varied while keeping the total amount of SnO_2 and mixed salts constant. Five experimental groups were set up, namely CsCl:KI = 0:2, 1:2, 2:2, 2:1, and 2:0, while the total amount of SnO_2 and the mixed salts was strictly maintained at a constant. The growth morphology of each group was characterized by OM firstly, and the results are shown in Fig. 5. The results show that the growth characteristics of SnS_2, such a morphology, lateral size, and thickness, are strongly depend on the CsCl/KI ratio. Increasing the CsCl proportion promotes lateral growth, leading to larger lateral sizes and reduced thickness, consistent with the effect of CsCl alone. In contrast, a higher KI content (CsCl:KI = 0:2 or 1:2) results in smaller lateral

sizes but smoother edges, clearer contours, and a pronounced triangular morphology, aligning with the high crystallinity and regularity achieved with KI alone. To address this, the atomic force microscopy (AFM) of SnS_2 growth with assistant of the KI, CsCl and KI/CsCl (KI:CsCl = 1:1) were performed and the results are shown in Fig. S2. For SnS_2 nanosheets grown with KI assistance, the average edge length is 34.4 μm, the average thickness is 26.0 nm, and the edges are smooth. In contrast, SnS_2 nanosheets grown with CsCl assistance exhibit a significantly larger average edge length of 155.1 μm, a considerably smaller average thickness of 3.7 nm, but with rough edges. When a mixed salt (KI/CsCl) is used, the resulting SnS_2 nanosheets show an average edge length of 66.3 μm, an average thickness of 10.6 nm, and smooth edges. Thus, CsCl promotes lateral expansion and thinning, while KI enhances morphological regularity and crystalline quality. In summary, the CsCl/KI ratio synergistically regulates the lateral and vertical growth rates of SnS_2, jointly determining its overall morphology and crystalline properties.

To gain mechanistic insight into how CsCl promotes lateral growth and KI improves morphology, theoretical calculations were performed as shown in Fig. S3. First-principles calculations reveal that the formation energies of SnS_2 on the (100), (010), and (001) planes are 0.0339 eV, 0.0339 eV and 0.0457 eV, respectively. The equal formation energies of the (100) and (010) planes are consistent with the sixfold symmetric structure of SnS_2. Notably, the formation energies of the in-plane (100) and (010) planes are lower than that of the out-of-plane (001) plane, indicating that 2D growth is energetically favorable. When Cs and K ions are introduced onto the (100), (010), and (001) surfaces of SnS_2, the binding energies on the (001) surface are the lowest for both ions, suggesting a preferential adsorption on this basal plane. This promotes lateral growth, which is in good agreement with experimental observations. Furthermore, the binding energy of Cs^+ on the (001) surface is lower than that of K^+, indicating that Cs^+ is more effective than K^+ in promoting lateral growth and thus facilitating the formation of thinner SnS_2 nanosheets. Additionally, the binding energies of Cs^+ on the (100) and (010) surfaces are lower than those of K^+, implying that K^+ exhibits weaker binding on these edge planes. This weaker interaction favors the formation of well-defined, sharp edges, consistent with the experimental observation that KI-assisted growth yields more regular morphologies. These theoretical results are in strong agreement with the experimental findings shown above. These findings provide important guidance for optimizing SnS_2 growth processes and preparing high quality samples.

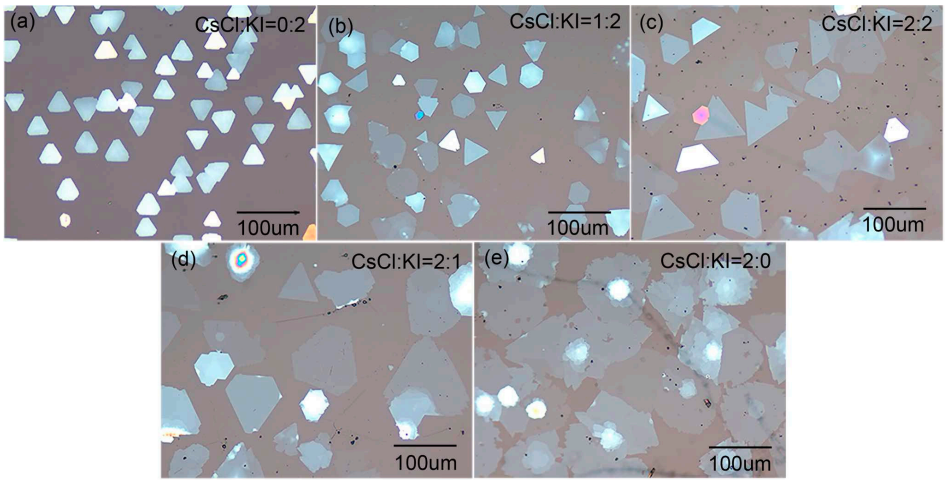

Figure 5: OM images of SnS_2 growth by mixed salt-assisted CVD. OM images of SnS_2 nanosheets grown with CsCl:KI ratios of 0:2 (**a**), 1:2 (**b**), 2:2 (**c**), 2:1 (**d**), and 2:0 (**e**), respectively.

3.2 Morphological and Chemical Composition Characterization

To systematically characterize the morphology, structure, and chemical composition of the ultrathin large-size SnS_2 nanosheets, atomic force microscopy (AFM), X-ray diffraction (XRD) and X-ray photoelectron spectroscopy (XPS) were employed. As shown in Fig. 6a, the lateral size of SnS_2 nanosheets can reach 248 μm when the salt mixing ratio (CsCl:KI = 2:2) is fixed and growth conditions are further optimized. AFM imaging (Fig. 6b) and cross-sectional analysis reveal a thickness of approximately 1.87 nm, confirming a bilayer structure [30]. XRD (Fig. 6c) exhibits distinct peaks at 14.9°, 30.2°, 46.0°, and 62.9°, corresponding to the (001), (002), (003), and (004) planes of SnS_2 (PDF#23-0677), respectively. No secondary phases are detected, confirming the single-phase nature of the as-prepared samples. The survey spectrum on as-grown mica substrate (Fig. 6d) reveals the expected Sn and S as, in addition to the weak C 1s peak always present at 284.8 eV for samples handled in air. Notably, Cs, Cl, K and I are clearly detected, and no other impurities are observed. While only Cs remains detectable, while K, Cl, and I are no longer observed after transfer to SiO_2/Si (Fig. S4). High-resolution XPS analysis (Fig. 6e–j) provides detailed chemical state information. The Sn 3d core level splits into two peaks at 495.1 eV and 486.6 eV due to spin-orbit coupling, corresponding to Sn $3d_{3/2}$ and Sn $3d_{5/2}$, respectively, indicating Sn in the Sn^{4+} state. The S 2p spectrum shows two peaks at 161.6 eV and 162.8 eV, assigned to S $2p_{3/2}$ and S $2p_{1/2}$, respectively, confirming sulfur in the S^{2-} state, these values are consistent with the previous reports [31]. The Cs 3d core level splits into two peaks at 738.6 eV and 724.6 eV, corresponding to Cs $3d_{3/2}$ and Cs $3d_{5/2}$, respectively, indicating Cs in the Cs^+ state; the Cl 2p spectrum shows two peaks at 199.0 eV and 197.6 eV, assigned to Cl $2p_{1/2}$ and Cl $2p_{3/2}$, confirming Cl in the Cl^- state [32]. The K 2p spectrum exhibits two peaks at 296.0 eV and 293.2 eV, corresponding to K $2p_{1/2}$ and K $2p_{3/2}$, confirming K in the K^+ state; the I 3d spectrum shows two peaks at 630.5 eV and 618.9 eV, assigned to I $3d_{3/2}$ and I $3d_{5/2}$, confirming I in the I^- state [33]. The clearly detection of Cs, Cl, K, and I further demonstrates that the mixed salt (CsCl/KI) plays an important role in regulating both the lateral and vertical growth rates of SnS_2. Collectively, these results confirm that the as-grown SnS_2 nanosheets are of high quality.

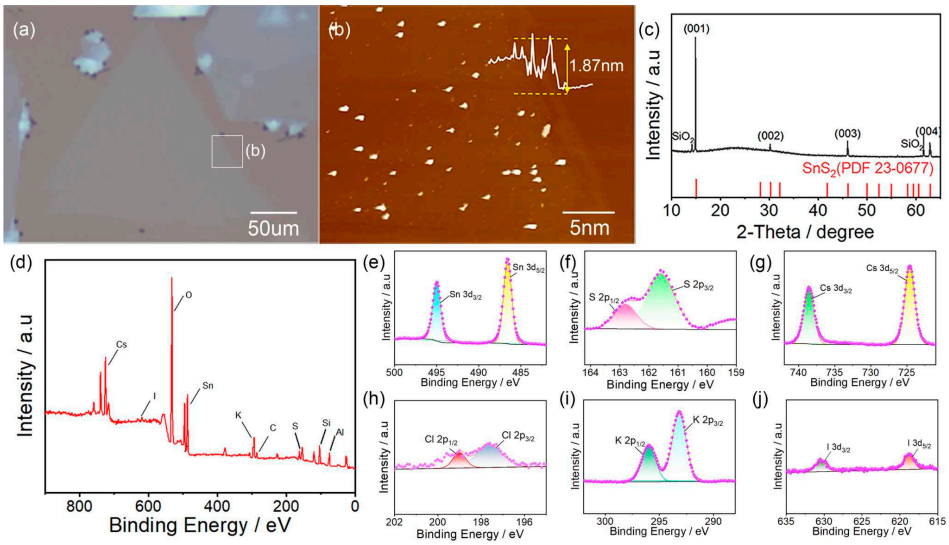

Figure 6: Morphological and compositional characterization of SnS_2 nanosheets. (**a**–**c**) OM image, AFM image, and XRD pattern of SnS_2 nanosheets, respectively; (**d**) XPS survey spectrum on as-grown mica substrate, confirming all expected elements; (**e**) Sn 3d region, fitted with a single spin-split doublet; (**f**) S 2p region, deconvoluted into two peaks; (**g**–**j**) Cs 3d, Cl 2p, K 2p, and I 3d regions, fitted with a single spin-split doublet.

3.3 Microstructure Characterization

To investigate the atomic-scale microstructure, growth orientation, and chemical composition distribution of SnS_2 nanosheets, transmission electron microscopy (TEM) was employed. Fig. 7a shows a TEM image of a transferred SnS_2 nanosheet, revealing its overall morphology. The high-resolution TEM (HR-TEM) image (Fig. 7b) reveals a hexagonal lattice structure free of atomic vacancies or lattice distortions. The measured lattice spacing is approximately 0.32 nm, matching the (100) interplanar spacing of standard SnS_2 (0.317 nm) and confirming the high crystal orientation. The selected area electron diffraction (SAED) pattern (Fig. 7c) exhibits regular hexagonal spots, confirming the hexagonal phase and excellent single-crystal quality of the as-prepared SnS_2 nanosheets. Moreover, energy-dispersive X-ray spectroscopy (EDS) elemental maps (Fig. 7d–f) show uniform distribution of Sn and S across the nanosheet, with no evidence of elemental segregation or enrichment.

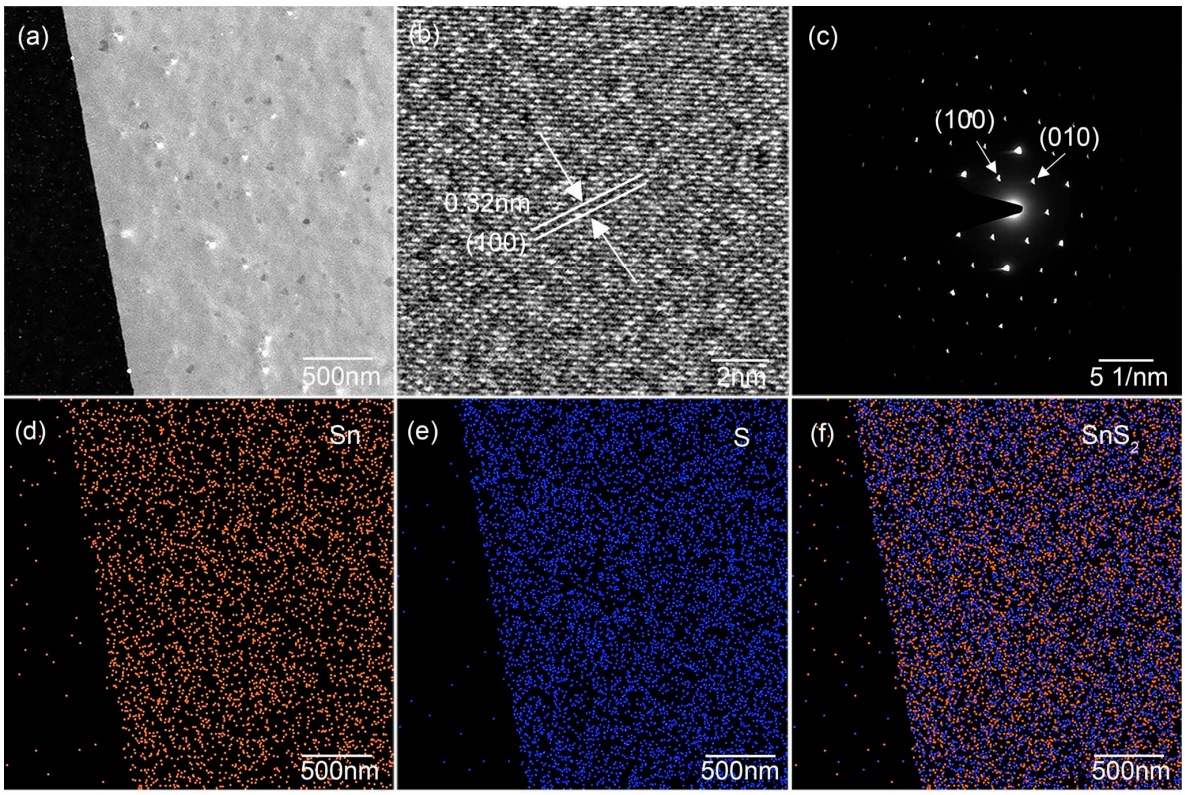

Figure 7: Atomic structure and chemical composition characterization of SnS_2 nanosheets. (**a**–**c**) TEM image, HR-TEM image, and SAED pattern of SnS_2 nanosheets, respectively; EDS elemental mapping of Sn (**d**), S (**e**), and SnS_2 (**f**).

3.4 Anisotropic Propertity

3.4.1 Angle-Resolved Polarized Raman Spectroscopy (ARPRS)

Raman spectroscopy utilizes scattered light to gain knowledge about molecular vibrations, which can provide information regarding the structure, symmetry, electronic environment, and chemical bonding of a material. This technique is highly sensitive to symmetry, crystallinity, and stress, making it a powerful tool for characterizing 2D materials. To further confirm that the interfacial stress originates from lattice mismatch between SnS_2 and the mica substrate, a series of control experiments were conducted. First, SnS_2 nanosheets were transferred onto different substrates, including Si, SiO_2/Si (300 nm SiO_2) and quartz glass.

Raman spectra of the SnS_2 nanosheets on both the as-grown (mica) and transferred substrates were then acquired, and the results are shown in Fig. S5. Notably, the characteristic Raman A_{1g} peak of SnS_2 on quartz glass, SiO_2/Si, and Si appears at 314.6 ± 0.4 cm^{-1}, 314.2 ± 0.2 cm^{-1}, and 314.1 ± 0.1 cm^{-1}, respectively, while on the as-grown mica substrate, it is located at 313.8 ± 0.03 cm^{-1}. Comparing the transferred substrates with the original growth substrate, a clear red-shift of the A_{1g} mode is observed. According to previous reports, the A_{1g} mode in SnS_2 is the primary out-of-plane vibrational mode [34,35]. Often described as a "breathing" vibration or an S-Sn-S stretching mode, it is known to be sensitive to applied stress or strain. Therefore, the observed red-shift of the A_{1g} mode on the as-grown substrate is indicative of the presence of stress [36,37]. To further investigate the effect of stress on the properties of SnS_2, the angle-resolved polarized Raman spectroscopy (ARPRS) of SnS_2 on the growth substrate and the transferred substrates were carried out and the results are shown in Fig. 8. Schematic diagrams of typical configurations for ARPRS are shown in Fig. 8a. For SnS_2 on SiO_2 (Fig. 8b–d), the Raman peak intensity remains nearly constant and exhibits no significant periodic variation with the polarization angle under parallel configuration (Fig. 8c). In contrast, under perpendicular configuration, the intensity is very low, nearly negligible (Fig. 8d). These observations indicate the intrinsic isotropy of SnS_2 [38]. These results are consistent with the calculations based on the semiclassical Placzek model and the corresponding Raman tensor [38,39]. Specifically, under parallel polarization, the Raman peak intensity remains constant and independent of the polarization angle, while it drops to zero under perpendicular polarization (see Supporting Information for details). This further confirms the intrinsic in-plane isotropy of SnS_2. In striking contrast, SnS_2 grown on mica exhibits a pronounced anisotropic response: both the mica peak at 263.8 cm^{-1} and the SnS_2 A_{1g} peak at 313.6 cm^{-1} display regular periodic intensity fluctuations with polarization angle (Fig. 8e), directly confirming strong anisotropy. Raman intensity color maps (Fig. 8f,g) clearly reveal the distribution of intensity. Further analysis shows that both the mica 263.8 cm^{-1} peak and the SnS_2 A_{1g} peak (313.6 cm^{-1}) exhibit a 90° periodic oscillation under parallel and perpendicular configurations. Polar plots (Fig. 8h) confirm that SnS_2 on SiO_2 shows no intensity variation with polarization angle, further supporting its isotropy. In contrast, SnS_2 growth on mica exhibits significant in-plane anisotropy (Fig. 8i–l). For the mica peak (263.8 cm^{-1}), maximum intensity occurs at 61°/151°/237°/325° (parallel) and 20°/108°/196°/288° (perpendicular). For the SnS_2 A_{1g} peak (313.6 cm^{-1}), maxima appear at 63°/150°/236°/325° (parallel) and 10°/101°/193°/289° (perpendicular). This periodic phenomenon is attributed to interfacial stress from lattice mismatch between SnS_2 and mica, which breaks the intrinsic hexagonal symmetry of SnS_2, resulting in pronounced in-plane anisotropy.

3.4.2 Polarized Optical Microscopy Characterization

To further verify the transition of SnS_2 nanosheets from isotropy to anisotropy, polarized optical imaging was employed [40]. As shown in Fig. 9a, for SnS_2 transferred onto SiO_2/Si (300 nm SiO_2), the SnS_2 brightness remains angle-independent and in an extinction state, indicating isotropy. In striking contrast, for SnS_2 grown directly on mica (Fig. 9b), its brightness displays a 90° periodic variation, with even greater amplitude than that of mica, confirming significant in-plane anisotropy. To enable quantitative analysis of the intensity-versus-angle relationship, polar plots of polarized reflected light intensity were constructed for SnS_2 both on the growth substrate and after transferred to SiO_2/Si. The polarized reflected light intensity from SnS_2 transferred to SiO_2/Si was very low and remained nearly constant as a function of the sample rotation angle θ (Fig. 9c). In contrast, SnS_2 on the original growth substrate exhibited a distinct four-folded periodic patterns, confirming the presence of strong in-plane optical anisotropy (Fig. 9d). In summary, combining ARPRS and polarized optical imaging, this study deepens the understanding of interfacial stress effects in 2D materials and demonstrates a strategy for converting intrinsically isotropic 2D materials

into anisotropic ones. This work provides important theoretical and experimental support for designing polarization-sensitive optoelectronic devices based on anisotropic SnS_2.

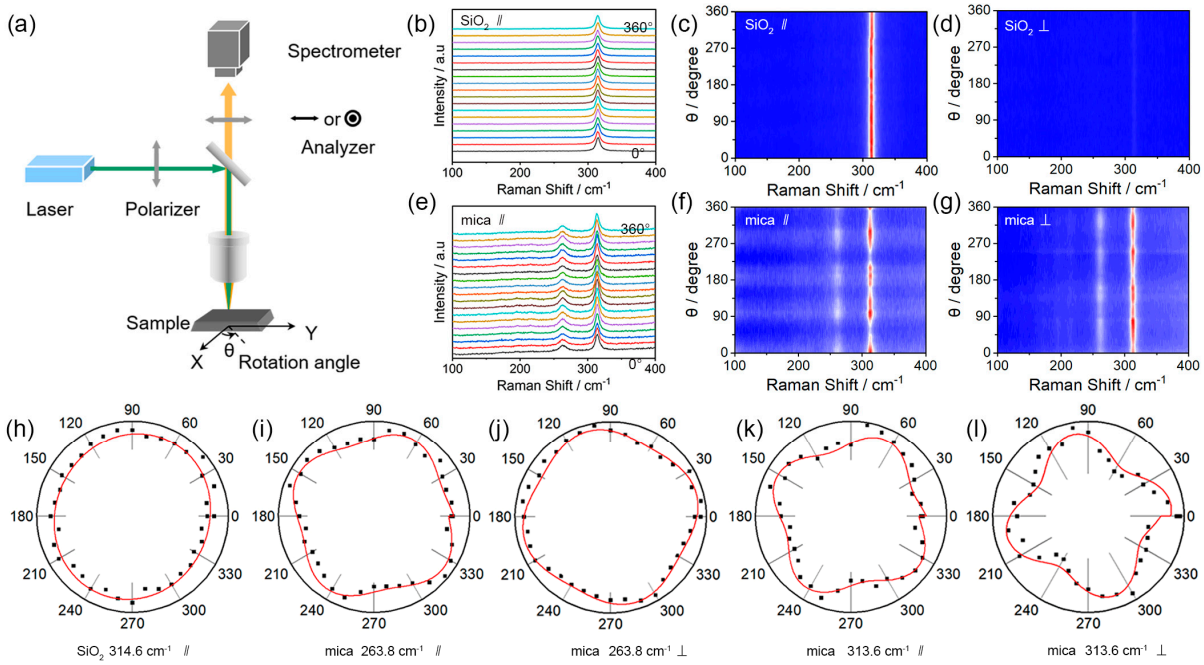

Figure 8: The ARPRS of the SnS_2 nanosheets. (**a**) Schematic diagrams of typical configurations for ARPRS. the ARPRS of the SnS_2 nanosheets transferred on SiO_2 (**b**) and grown on mica substrates (**e**) under parallel polarization configuration; False-color intensity maps for SnS_2 nanosheets transferred on SiO_2 under parallel (**c**) or perpendicular (**d**) polarization configuration, respectively; False-color intensity maps for SnS_2 nanosheets grown on mica substrates under parallel (**f**) or perpendicular (**g**) polarization configuration, respectively; Polar plots of the 314.6 cm^{-1} peak for SnS_2 nanosheets transferred on SiO_2 under parallel (**h**) polarization configuration. Polar plots of the 263.8 cm^{-1} (mica) and 313.6 cm^{-1} (SnS_2) peaks for SnS_2 nanosheets grown on mica substrates under parallel (**i**,**k**) or perpendicular (**j**,**l**) polarization configuration.

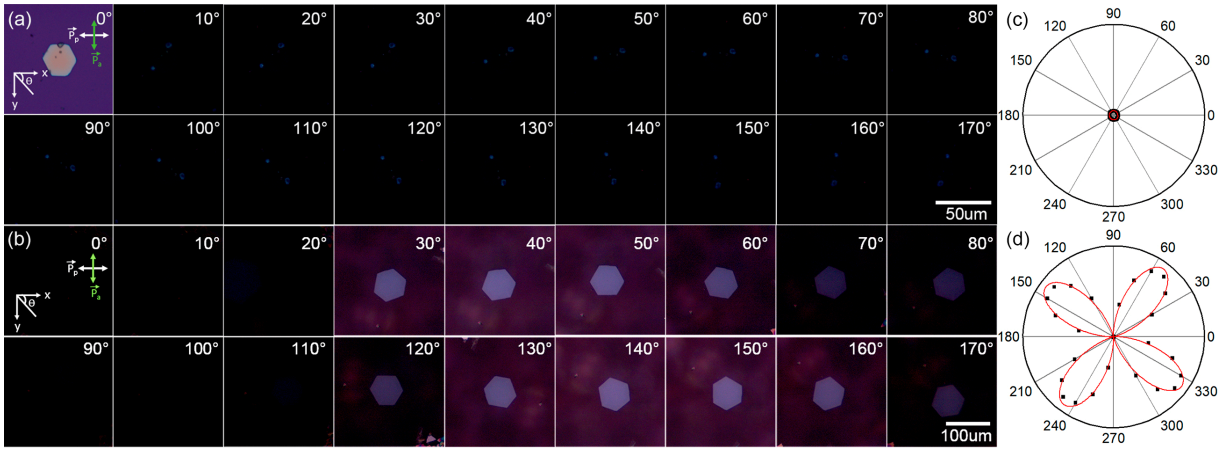

Figure 9: Polarized optical imaging of SnS_2 nanosheets. Polarized optical imaging of SnS_2 nanosheets after transferred to SiO_2/Si (**a**) (the ration angle of 0° is the optical microscopy image) and on the growth substrate (**b**); polar plots of polarized reflected light intensity of SnS_2 and after transferred to SiO_2/Si (**c**) and on the growth substrate (**d**).

4 Conclusion

This study focuses on the controllable synthesis and in-plane anisotropy modulation of 2D SnS_2 nanosheets. A CsCl/KI mixed salt-assisted growth strategy was used to synergistically control the morphology, lateral size, and thickness of the nanosheets. Experimental results show that CsCl promotes lateral growth, while KI optimizes crystal morphology. Using this mixed salt system, triangular, ultrathin, large-size SnS_2 nanosheets with a lateral size exceeding 200 μm and a thickness of only 1.8 nm were successfully fabricated. ARPRS reveals that SnS_2 nanosheets transferred onto SiO_2 substrates exhibit intrinsic in-plane isotropy. In contrast, for SnS_2 grown directly on mica, lattice mismatch induces interfacial stress that breaks the intrinsic symmetry, causing the A_{1g} Raman peak intensity to exhibit a 90° periodic variation with polarization angle, which demonstrates pronounced in-plane anisotropy and further confirmed by polarized optical microscopy. This work provides a new method for the controllable growth of SnS_2 nanosheets and offers experimental evidence for understanding stress-induced anisotropy in 2D materials.

Acknowledgement: Not applicable.

Funding Statement: This work was financially supported by the Natural Science Foundation of Fujian Province of China (2022J01646).

Author Contributions: Yulong Lian contributed to conceptualization, methodology, investigation, data curation and writing—original draft. Ruiqiang Wang contributed to methodology, formal analysis, validation, and visualization. Ziyan Ding contributed to investigation, resources, and validation. Jinyang Liu contributed to conceptualization, supervision, project administration, funding acquisition, and writing—review & editing. All authors reviewed and approved the final version of the manuscript.

Availability of Data and Materials: The data that support the findings of this study are available from the corresponding author upon reasonable request.

Ethics Approval: Not applicable.

Conflicts of Interest: The authors declare no conflicts of interest.

Supplementary Materials: The supplementary material is available online at https://www.techscience.com/doi/10.32604/cl.2026.083268/s1.

References

1. Kim KS, Kwon J, Ryu H, Kim C, Kim H, Lee EK, et al. The future of two-dimensional semiconductors beyond Moore's law. Nat Nanotechnol. 2024;19(7):895–906. [CrossRef].
2. Ren W, Bøggild P, Redwing J, Novoselov KS, Sun L, Qi Y, et al. The 2D materials roadmap. 2D Mater. 2026;13(2):021501. [CrossRef].
3. Xu H, Xu Z, Ren Q, Meng Y, Han S, Wang Z, et al. Two-dimensional materials for integrated sensing. Nat Mater. 2026:1–15. [CrossRef].
4. Wu R, Zhang H, Ma H, Zhao B, Li W, Chen Y, et al. Synthesis, modulation, and application of two-dimensional TMD heterostructures. Chem Rev. 2024;124(17):10112–91. [CrossRef].
5. Zhan S, Zheng L, Xiao Y, Zhao LD. Phonon and carrier transport properties in low-cost and environmentally friendly SnS_2: A promising thermoelectric material. Chem Mater. 2020;32(24):10348–56. [CrossRef].
6. Gong Y, Yuan H, Wu CL, Tang P, Yang SZ, Yang A, et al. Spatially controlled doping of two-dimensional SnS_2 through intercalation for electronics. Nat Nanotechnol. 2018;13(4):294–9. [CrossRef].
7. Mishra RK, Choi HJ, Ryu JW, Choi GJ, Kumar V, Kumar P, et al. Recent progress in gas sensing based on 2D SnS_2 and its heterostructure platforms: A review. Sens Actuat A Phys. 2024;365:114860. [CrossRef].

8. Guo X, Zhang F, Zhang Y, Hu J. Review on the advancement of SnS_2 in photocatalysis. J Mater Chem A. 2023;11(14):7331–43. [CrossRef].
9. Li B, Xing T, Zhong M, Huang L, Lei N, Zhang J, et al. A two-dimensional Fe-doped SnS_2 magnetic semiconductor. Nat Commun. 2017;8:1958. [CrossRef].
10. Huang Y, Sutter E, Sadowski JT, Cotlet M, Monti OLA, Racke DA, et al. Tin disulfide—An emerging layered metal dichalcogenide semiconductor: Materials properties and device characteristics. ACS Nano. 2014;8(10):10743–55. [CrossRef].
11. Gao P, Wang L, Zhang YY, Huang Y, Liao L, Sutter P, et al. High-resolution tracking asymmetric lithium insertion and extraction and local structure ordering in SnS_2. Nano Lett. 2016;16(9):5582–8. [CrossRef].
12. Masood N, Toufiq AM, Magam S, Ali SMW, Qureshi MT. Structural and electrochemical properties of flower-like SnS_2 architectures as cathodic material for lithium-sulfur batteries. Chalcogenide Lett. 2025;22(12):1047–53. [CrossRef].
13. Dai Y, Huang X, Han X, Guo J, Xu X, Wang L, et al. Recent progress of mechanical exfoliation and the application in the study of 2D materials. In: Two-dimensional transition-metal dichalcogenides: Phase engineering and applications in electronics and optoelectronics. Hoboken, NJ, USA: Wiley Semiconductors; 2024. p. 211–65. [CrossRef].
14. Song O, Kang J. Solution-processed 2D materials for electronic applications. ACS Appl Electron Mater. 2023;5(3):1335–46. [CrossRef].
15. Sun L, Yuan G, Gao L, Yang J, Chhowalla M, Gharahcheshmeh MH, et al. Chemical vapour deposition. Nat Rev Meth Primers. 2021;1:5. [CrossRef].
16. Abimaheshwari R, Abinaya R, Prasanna CS, Navaneethan M, Harish S. Dynamic growth configuration of 2D-SnS_2 nanoflakes for humidity-resistant NO_2 monitoring system: Mechanistic insights and environmental applications. Small. 2025;21(33):2504996. [CrossRef].
17. Koyama K, Ishihara J, Matsui N, Mori A, Li S, Yang J, et al. Selective synthesis of large-area monolayer tin sulfide from simple substances. Nano Lett. 2025;25(25):9985–93. [CrossRef].
18. Zhou X, Zhang Q, Gan L, Li H, Zhai T. Large-size growth of ultrathin SnS_2 nanosheets and high performance for phototransistors. Adv Funct Mater. 2016;26(24):4405–13. [CrossRef].
19. Ye G, Gong Y, Lei S, He Y, Li B, Zhang X, et al. Synthesis of large-scale atomic-layer SnS_2 through chemical vapor deposition. Nano Res. 2017;10(7):2386–94. [CrossRef].
20. Wang Z, Pang F. In-plane growth of large ultra-thin SnS_2 nanosheets by tellurium-assisted chemical vapor deposition. RSC Adv. 2017;7(46):29080–7. [CrossRef].
21. Liu XX, He DW, He JQ, Wang YS, Fu M. Chemical vapor deposition growth of crystal monolayer SnS_2 with NaCl-assistant. Chin Phys B. 2019;28(11):118101. [CrossRef].
22. Shao G, Xue XX, Zhou X, Xu J, Jin Y, Qi S, et al. Shape-engineered synthesis of atomically thin 1T-SnS_2 catalyzed by potassium halides. ACS Nano. 2019;13(7):8265–74. [CrossRef].
23. Fu Q, Wu Q, Zhang X, Cai Z, Ostrikov KK, Gu X, et al. One-step epitaxial growth of multilayer MoS_2/SnS_2 vertical nanosheets for high-performance photodetectors. ACS Appl Nano Mater. 2022;5(10):14978–86. [CrossRef].
24. Xia J, Zhu D, Wang L, Huang B, Huang X, Meng XM. Large-scale growth of two-dimensional SnS_2 crystals driven by screw dislocations and application to photodetectors. Adv Funct Mater. 2015;25(27):4255–61. [CrossRef].
25. Li M, Zhu Y, Li T, Lin Y, Cai H, Li S, et al. One-step CVD fabrication and optoelectronic properties of SnS_2/SnS vertical heterostructures. Inorg Chem Front. 2018;5(8):1828–35. [CrossRef].
26. Wu Y, Liu J, Lian Y, Lian Y, Cai H. Sb_2Se_3 mutisegment homostructured nanowire growth with a catalyst-free incommensurate heteroepitaxial method. Cryst Growth Des. 2025;25(8):2588–95. [CrossRef].
27. Liu J, Wu Y, Lian Y, Lian Y, Lin Z, Cai H, et al. The polarization-resolved and helicity-resolved Raman spectroscopy of the twisted 1D/2D MoO_2 mixed-dimensional homojunction. ACS Appl Mater Interfaces. 2025;17(31):44719–27. [CrossRef].
28. Li S. Salt-assisted chemical vapor deposition of two-dimensional transition metal dichalcogenides. iScience. 2021;24(11):103229. [CrossRef].
29. Wang Y, Huang L. Recent advances in salt-assisted synthesis of 2D materials. Small. 2025;21(5):e2410028. [CrossRef].

30. Sriv T, Kim K, Cheong H. Low-frequency Raman spectroscopy of few-layer 2H-SnS_2. Sci Rep. 2018;8:10194. [CrossRef].
31. Peheliwa VM, Lu KC, Hasibuan DP, Saragih CS, Maria CCS, Chen YR, et al. Layer-dependent optical modulation and field-effect-transistor in two-dimensional 4H-SnS_2 layers. Adv Opt Mater. 2023;11(17):2300395. [CrossRef].
32. Škorjanc V, Miaskiewicz A, Roß M, Maniyarasu S, Severin S, Leyden MR, et al. Seed layers for wide-band gap coevaporated perovskite solar cells: CsCl regulates band gap and reduces process variability. ACS Energy Lett. 2024;9(11):5639–46. [CrossRef].
33. Li N, Qin S, Hao Y, Wang X, Chang T, Liu X, et al. Nanoarchitectonics of polymeric crown-ether analog of Tröger base combined with potassium iodide and acids synergy in fixation of CO_2 and epoxides. Mol Catal. 2023;545:113241. [CrossRef].
34. Xu L, Zhang P, Jiang H, Wang X, Chen F, Hu Z, et al. Large-scale growth and field-effect transistors electrical engineering of atomic-layer SnS_2. Small. 2019;15(46):e1904116. [CrossRef].
35. Gonzalez JM, Oleynik II. Layer-dependent properties of SnS_2 and $SnSe_2$ two-dimensional materials. Phys Rev B. 2016;94(12):125443. [CrossRef].
36. Ram B, Singh AK. Strain-induced indirect-to-direct band-gap transition in bulk SnS_2. Phys Rev B. 2017;95(7):075134. [CrossRef].
37. Liu X, Deng X, Li X, Chiu HC, Chen Y, Botcha VD, et al. Impact of Al_2O_3 stress liner on two-dimensional SnS_2 nanosheet for photodetector application. J Alloys Compd. 2020;830:154716. [CrossRef].
38. Ding Y, Zheng W, Lu X, Liang Y, Zhu Y, Jin M, et al. Raman tensor of layered SnS_2. J Phys Chem Lett. 2020;11(23):10094–9. [CrossRef].
39. Loudon R. The Raman effect in crystals. Adv Phys. 1964;13(52):423–82. [CrossRef].
40. Zhang J, Zhao G, Hao Z, Huo J, Li H, Kozadaev K, et al. Twist-induced giant modulation of optical and optoelectronic anisotropy in van der Waals $NbOX_2$ homo-/heterostructures. Nano Lett. 2026;26(1):482–90. [CrossRef].